Molecular mechanism of the severe MH/CCD mutation Y522S in skeletal ryanodine receptor (RyR1) by cryo-EM

Kavita A. Iyer[a] [iD], Yifan Hu[a], Thomas Klose[b] [iD], Takashi Murayama[c] [iD], and Montserrat Samsó[a,1] [iD]

Ryanodine receptors (RyRs) are main regulators of intracellular Ca^{2+} release and muscle contraction. The Y522S mutation of RyR1 causes central core disease, a weakening myopathy, and malignant hyperthermia, a sudden and potentially fatal response to anesthetics or heat. Y522 is in the core of the N-terminal subdomain C of RyR1 and the mechanism of how this mutation orchestrates malfunction is unpredictable for this 2-MDa ion channel, which has four identical subunits composed of 15 distinct cytoplasmic domains each. We expressed and purified the RyR1 rabbit homolog, Y523S, from HEK293 cells and reconstituted it in nanodiscs under closed and open states. The high-resolution cryogenic electron microscopic (cryo-EM) three-dimensional (3D) structures show that the phenyl ring of Tyr functions in a manner analogous to a "spacer" within an α-helical bundle. Mutation to the much smaller Ser alters the hydrophobic network within the bundle, triggering rearrangement of its α-helices with repercussions in the orientation of most cytoplasmic domains. Examining the mutation-induced readjustments exposed a series of connected α-helices acting as an ~100 Å-long lever: One end protrudes toward the dihydropyridine receptor, its molecular activator (akin to an antenna), while the other end reaches the Ca^{2+} activation site. The Y523S mutation elicits channel preactivation in the absence of any activator and full opening at 1.5 μM free Ca^{2+}, increasing by ~20-fold the potency of Ca^{2+} to activate the channel compared with RyR1 wild type (WT). This study identified a preactivated pathological state of RyR1 and a long-range lever that may work as a molecular switch to open the channel.

ryanodine receptor | malignant hyperthermia | central core disease | calcium channel | excitation–contraction coupling

Ryanodine receptors (RyRs) are homotetrameric calcium channels of 2.26 MDa molecular weight located intracellularly in the membrane of the sarcoplasmic reticulum (SR), which act as gatekeepers of Ca^{2+} stores and are indispensable for muscle contraction and signaling events. The activity of the skeletal muscle isoform, RyR1, is under stringent control of the voltage-gated dihydropyridine receptor (DHPR) via conformational coupling. Although the molecular details of the tight interaction between the two proteins are still not fully understood, sarcolemmal depolarization activates DHPR, triggering activation of RyR1 and subsequent release of stored Ca^{2+}, resulting in muscle contraction. These sequential steps constitute pivotal events in excitation–contraction (EC) coupling. The signal from released Ca^{2+} is terminated via recycling of Ca^{2+} into the SR by sarco/endoplasmic reticulum calcium-ATPase (SERCA) pumps (1–3).

Mutations in RyR1 are a major cause of congenital myopathies, including malignant hyperthermia (MH) and central core disease (CCD) (4–6). MH is triggered when susceptible individuals with mutations in RyR1 are exposed to volatile anesthetics such as halothane and is characterized by muscular rigidity and spasms, hyperthermia, and rhabdomyolysis (7), which can be fatal if not treated promptly with the muscle relaxant dantrolene (7–9). CCD is characterized by chronic hypotonia, motor developmental delays, and orthopedic complications (10, 11).

One of the first MH/CCD-causing mutations identified was a single point Tyr-to-Ser (Y522S) mutation (12), which additionally can cause life-threatening susceptibility to environmental heat (13). This mutation is one of the harshest by several metrics (14, 15), with lethal homozygous expression (7, 16). Ryanodine binding experiments indicate high probability of opening across the 2 to 7 pCa range (13) and functional characterization of RyR1 Y522S in cultured myotubes shows an exacerbated SR Ca^{2+} leak, leading to SR depletion and elevated cytoplasmic Ca^{2+} concentration at rest (13–15). A singular feature of this mutation is the activation of mutant RyR1 starting at much more hyperpolarized potentials (~40 mV) than RyR1 wild type (WT) (15), suggesting altered interaction with the DHPR. Currently, there are no structural data explaining the underlying molecular mechanism of this mutation. Located in the N-terminal subdomain C (NTDC; residues

Significance

Skeletal muscle contraction is governed by ryanodine receptor 1 (RyR1) channels. Ryanodine receptors (RyRs) are the largest ion channels known, with multiple interconnected regulatory domains. Single point mutations of RyRs cause life-threatening diseases, and understanding their underlying molecular mechanism requires interpretation within the full protein context. Our cryo-EM reconstructions of the severe RyR1 Y523S mutation (in rabbit; corresponding to human Y522S) under open and closed states reveal widespread and far-reaching conformational changes transmitted over multiple domains that result in preactivation of the channel and suggest altered communication with RyR1's partner protein, the dihydropyridine receptor. The mutation reveals correlations between distinctive structural traits and functional anomalies and provides insight into the future design of therapies to modulate RyRs.

[1]To whom correspondence may be addressed. Email: montserrat.samso@vcuhealth.org.

394 to 631) of RyR1, the residue of interest, Tyr522, is cocooned by four neighboring α-helices of the NTDC, whose one end protrudes toward the T-tubule membrane, constituting one of the closest RyR1 domains approaching the DHPR complex. The long molecular distances from the mutated residue to the pore (120 Å) and to the Ca^{2+}-sensing site (65 Å), along with the significantly altered communication with the DHPR, suggest a more robust structural modification as a consequence of this single point mutation. Being located in the interior of a domain, a simple explanation such as disruption of an interdomain interaction would not be plausible.

Here, we studied the molecular mechanism of the $522^{Tyr-to-Ser}$ single point mutation by determining the structure of full-length rabbit RyR1 with the equivalent mutation, Y523S, embedded in nanodiscs under closed and open states using cryogenic electron microscopy (cryo-EM). Comparison with our previously determined three-dimensional (3D) structure of an NTDA RyR1 mutant (R164C) (17) using detailed tailored metrics for RyR revealed a completely different mechanism with greater conformational changes. We found that the molecular mechanism led to a common "domino-like effect" underlying the leakiness of mutant RyR1 that also affected the surface facing toward the DHPR. Cryo-EM characterization of this RyR1 mutant under open- and closed-state conditions uncovered an intramolecular lever acting over long distances and a distinct mechanism for this severe mutation; and furthermore, it demonstrated a physiologically relevant mechanism of RyR1 activation in skeletal muscle.

Results

High-resolution structural determination of the mutant RyR1 required a homotetrameric channel; the lethality of this mutation, however, prevents homozygous expression (7, 16). Thus, recombinant homotetrameric rabbit RyR1 Y523S was expressed stably in HEK293 cells using the Flp-In T-REx system and a doxycycline-inducible promoter as previously reported (18, 19). RyR1s were purified using sucrose density gradient centrifugation (20), supplemented with FKBP12.6, and reconstituted into nanodiscs under either closed-state (2 mM ethyleneglycol- bis(β-aminoethyl)-N,N,N′,N′-tetraacetic acid; EGTA, i.e., submicromolar free Ca^{2+}) or open-state (1.5 μM free Ca^{2+}, 5 mM adenosine 5′-triphosphate; ATP) conditions (*SI Appendix*, Table S1). Cryo-EM yielded 3D reconstructions of the mutant RyR1 at global resolutions of 4.0 and 4.1 Å, for the closed- and open-state conditions, respectively (*SI Appendix*, Figs. S1–S4). Classification did not yield any additional closed or "primed" states (*SI Appendix*, Fig. S5) as seen previously for RyR1 WT under open-state conditions (21). For the reconstruction obtained under closed-state conditions, further improvement in map quality was achieved by local refinement using a mask for a single monomer of RyR1 as well as particle subtraction and local refinement focused on the NTD (A to C) and SPRY (1 to 3) domains (*SI Appendix*, Fig. S1).

Homotetrameric RyR1 Y523S had a well-preserved structure and exhibited the characteristic square shape of the cytoplasmic assembly (CytA) (270 Å × 270 Å) (*SI Appendix*, Fig. S3). The transmembrane domain (TmD), consisting of six transmembrane helices (S1–S6) per monomer, emerges from the CytA and resembles a stalk-like structure (*SI Appendix*, Fig. S6). The nanodisc wrapped around the bundle of TmD helices in the form of two belts (a tighter upper belt and a looser lower belt). We observed densities corresponding to lipids occupying crevices within the TmD as described in the section pertaining to the pore of the channel. For the comparative analyses, we used the structures of rabbit RyR1 WT previously solved in closed- and open-state conditions (PDB: 5TB0 and 5TAL, respectively) (21).

The changes consist of large-scale intra- and intersubunit rearrangements across multiple domains of the CytA as a direct consequence of local changes at the mutation site. We describe in greater detail next the conformational changes in the mutant RyR1: 1) under closed-state conditions with a closed pore, henceforth referred to as quasi-open; and 2) under open-state conditions with an open pore, henceforth referred to as open⁺.

Quantification of Large-Scale Conformational Changes Induced by Y523S. Channel opening in RyR1 involves the concerted movement of most domains within the enormous square prism-shaped CytA, resulting in separation of pore-lining helices (S6) (nomenclature as previously defined in ref. 1) (*SI Appendix*, Fig. S6). The peripheral regions of the CytA (e.g., HD1) move downward as the domains facing the fourfold axis move upwards, ultimately pulling the C-terminal domain (CTD) in a way that forces the S6 helices to separate. This conformational change allows Ca^{2+} to pass through the channel. This well-documented conformational change (21–23), also termed "flexion" (24), takes place in the mutant channel, not only in the open state but also in the closed state.

To demonstrate and quantify the conformational changes caused by the Y523S mutation, we created heat maps of the rotation and translation of each domain within a monomer of RyR1 using the WT closed state as a reference (Fig. 1). Under closed-state conditions, the heat maps indicate that domains of CytA in the vicinity of the Y523S mutation exhibited relocations (more so in terms of rotation than translation) akin to those measured during WT RyR1 channel opening (Fig. 1). The increased flexion of the CytA was evident from the ~8° rotation of both HD1 and NTDB in the quasi-open channel, of the same magnitude as the WT opening. Moreover, Y523S under open-state conditions further exaggerated the opening motion, with rotations of ~10° for the same domains (Fig. 1).

NTDC, the domain containing the mutation of interest, exhibited a rotation of ~5° and translation of ~2 Å in the quasi-open structure, which indicates that the domain moved almost all the way to the channel opening (Fig. 1). Strikingly, the P1 domain (residing at the very corners of RyR1) exhibited a rotation of 7.0° in RyR1 Y523S (closed state), which was 2.0° greater than the 5.0° observed upon the WT RyR1 channel opening (Fig. 1). Additionally, NTD subdomain A (NTDA), NTD subdomain B (NTDB), and helical domain 1 (HD1), which are in contact with NTDC, exhibited rotations comparable to those seen during the RyR1 WT opening (Fig. 1). The long and curved HD2 domain, which protrudes from the corners of the CytA near NTDC and returns to it near SPRY2 of the adjacent subunit, underwent drastic conformational changes. Although its large size and elasticity prevented measurement of absolute rotation and translation values, HD2 exhibited the greatest translation (Fig. 2), contributing to the large tilt of SPRY2. Finally, the remaining domains of the CytA (SPRY3 and handle domains) exhibited relocations of smaller magnitude in the quasi-open conformation. Overall, the conformational changes ranged from comparable to lesser than those observed during WT channel opening. Nevertheless, they were considerable (Figs. 1 and 2) and appeared sufficient to be consequential (Fig. 2). The central domain (CD), which functions as an intermediary between CytA and TmD, tilted one-third of the way in RyR1 Y523S quasi-open with respect to WT channel opening (Fig. 1). Analysis of the individual helices of the TmD shows that its helices S1–S5 moved considerably in RyR1 Y523S quasi-open (Figs. 1 and 2).

Under open-state conditions, RyR1 Y523S open⁺ exhibited greater movements than during WT opening for a vast majority of domains both in terms of rotation (especially for NTDA–C,
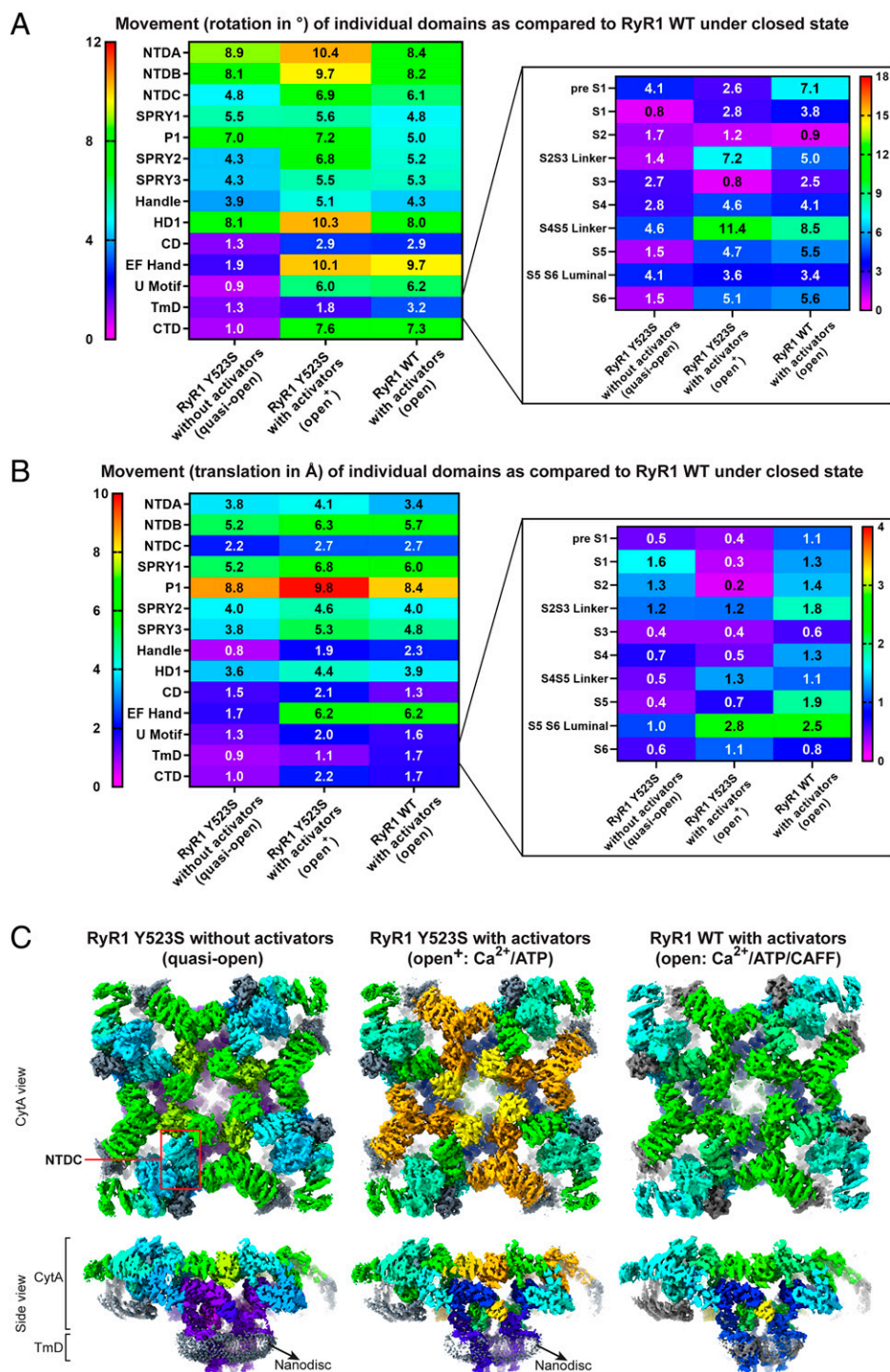
Fig. 1. Large-scale domain movements (rotation and translation) in RyR1 Y523S. (*A* and *B*) Rainbow heat maps of domain movements quantified in RyR1 Y523S quasi-open, RyR1 Y523S open+, and RyR1 WT open. Domains are colored from violet to red, with larger magnitude of movements (rotation in degrees [°] and translation in angstroms [Å]) colored red. All measurements were performed with respect to RyR1 WT closed (PDB: 5TB0). (*C*) Individual domains in the cryo-EM maps of RyR1 Y523S quasi-open, RyR1 Y523S open+, and RyR1 WT open (PDB: 5TAL) are color-coded according to magnitude of rotation with respect to RyR1 WT closed (PDB: 5TB0). Helical domain 2 (HD2) and FKBP12.6 in each cryo-EM map are colored gray.

SPRY1 and 2, P1, handle, and HD1), as well as in terms of translation (notably for NTDA, NTDB, SPRY1, P1, HD1, CD, U-motif, and CTD) (Figs. 1 and 2). In addition, the S2–S3 linker as well as the S4–S5 linker in the TmD also rotated more than in the RyR1 WT open structure (Fig. 1).

The Mutation Alters the DHPR-Facing Surface of RyR1. NTDC, the domain harboring the mutation, is formed by a helical bundle core (helices h_4–h_8) protruding toward the DHPR and

additional helices h_1–h_3, with h_3 penetrating deeper into the CytA (Fig. 3 and sequence demarcations in *SI Appendix,* Fig. *S7A*). Analysis of the Tyr-to-Ser mutant revealed a 4.8° overall rocking of the NTDC under closed-state conditions, which approached the 6.1° motion that this domain undergoes upon opening in WT. Opening of the mutant channel resulted in rocking of 6.9° (Fig. 3*A*). In all cases, rocking takes place around a pivot point in NTDC's third helix (h_3), which undergoes more tilt when considered alone: in mutant RyR1 under
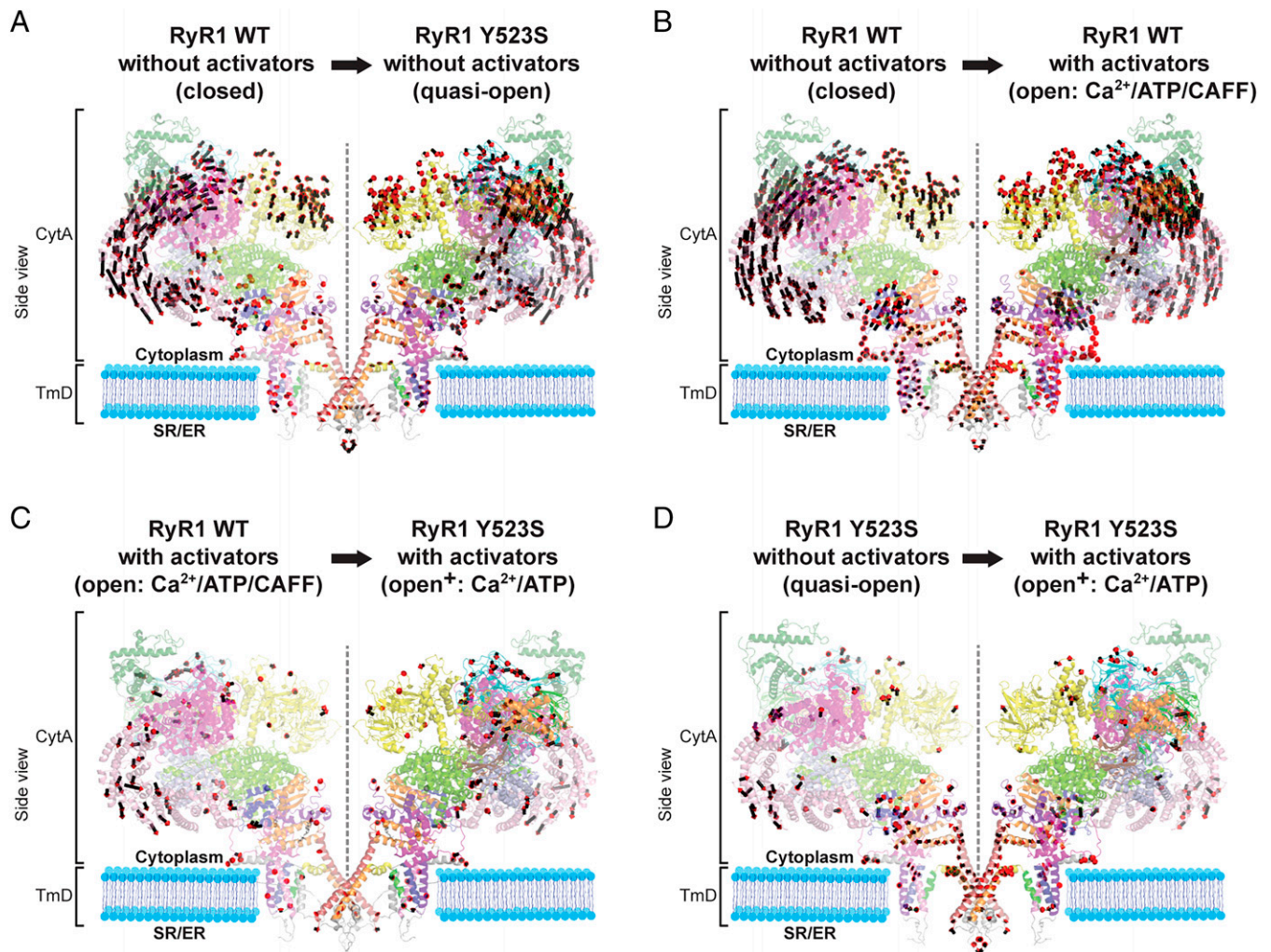
Fig. 2. Vector arrows highlight movements of individual domains in RyR1. (*A*) The Y523S mutation causes conformational changes in the CytA that radiate across several domains as shown by the vector arrows (red arrowhead, black tail). Changes of smaller magnitude were also observed in the TmD. (*B*) Upon WT channel opening, the CytA undergoes downward motion at the periphery and upward motion at the center along with separation of pore lining helices allowing conductance of Ca^{2+} from the SR/ER into the cytoplasm. (*C*) Presence of vector arrows scattered throughout the CytA and TmD in the RyR1 in the presence of activators (Ca^{2+} and ATP) indicate that the mutant RyR1 Y523S channel is open to a greater extent than open WT. (*D*) Sparsity of vector arrows in the CytA of RyR1 Y523S quasi-open when compared to the open$^+$ structure reveals that the CytA of the quasi-open structure, despite being under closed-state conditions, has already undergone considerable conformational changes necessary for channel opening except for separation of the TmD pore-lining helices (indicated by the clustering of vector arrows in that area). For clarity only two monomers of RyR1 in diagonal are shown as transparent ribbons with individual domains color coded (*SI Appendix*, Fig. S5). The dashed gray line indicates the fourfold axis.

closed-state conditions (i.e., quasi-open), h_3 pivots 5.8° such that its upper half rocks away from the CD and the fourfold axis while its lower half pushes toward them, nearing the 7.2° motion that takes place in the WT channel opening. In comparison, mutant open$^+$ exhibits additional motion, to 7.9° (Fig. 3*B* and *SI Appendix*, Fig. S8 and Movie S1). While the angle for the entire NTDC and h_3 differs due to their differing geometry, both measurements attest to the quasi-open conformation of the mutant channel under closed-state conditions as well as a conformation beyond the open state (open$^+$) for the mutant channel under open-state conditions. The rearrangement of the NTDC core, which protrudes from the surface of RyR1 toward the DHPR, could explain the altered communication with the DHPR, to which RyR1 is conformationally coupled.

Understanding the conspicuous reorientation of the NTDC caused by the mutation alone requires a closer look at the immediate vicinity of the mutation site. Tyr523 is located in the middle of NTDC's fifth helix (h_5) and interacts with a number of hydrophobic residues (Ile491, Val519, Leu522, Leu526, Trp546, Ile560, and Val563) that are contributed by its four neighboring

α-helices (h_4, h_6, h_7, and h_8) (Fig. 3 and *SI Appendix*, Fig. S7). The WT channel opening does not alter the relative orientation of its $h_{4–8}$ α-helices, since hydrophobic interactions between Tyr523 and neighboring residues are preserved (Fig. 3 and *SI Appendix*, Fig. S7A). Mutation to the smaller, polar Ser residue, however, abolishes the favorable interactions with all of the previously mentioned hydrophobic residues (*SI Appendix*, Fig. S7A) and alters the relative orientations of the four surrounding helices (h_4 and $h_{6–8}$) with respect to helix h_5, the helix that contains the mutation (Fig. 3*C* and *SI Appendix*, Fig. S7A). The mutation induces two significant local effects: 1) Absence of the bulky Tyr523 allows forward sliding of h_4, becoming out of register with respect to h_5; this in turn results in a reorientation of h_3, which rocks and is dragged upward (Fig. 3*B*). 2) Concomitantly, Phe540 in helix h_7 is forced into an altered conformation due to the mutation and becomes better sandwiched within the helical bundle; this positioning results in strengthened favorable interactions with Leu488 and Leu484 of helix h_4; Leu526 and Ile530 of helix h_5; and Val567 of helix h_8 (*SI Appendix*, Fig. S7B). These conformational changes resulted in the loss of a kink between
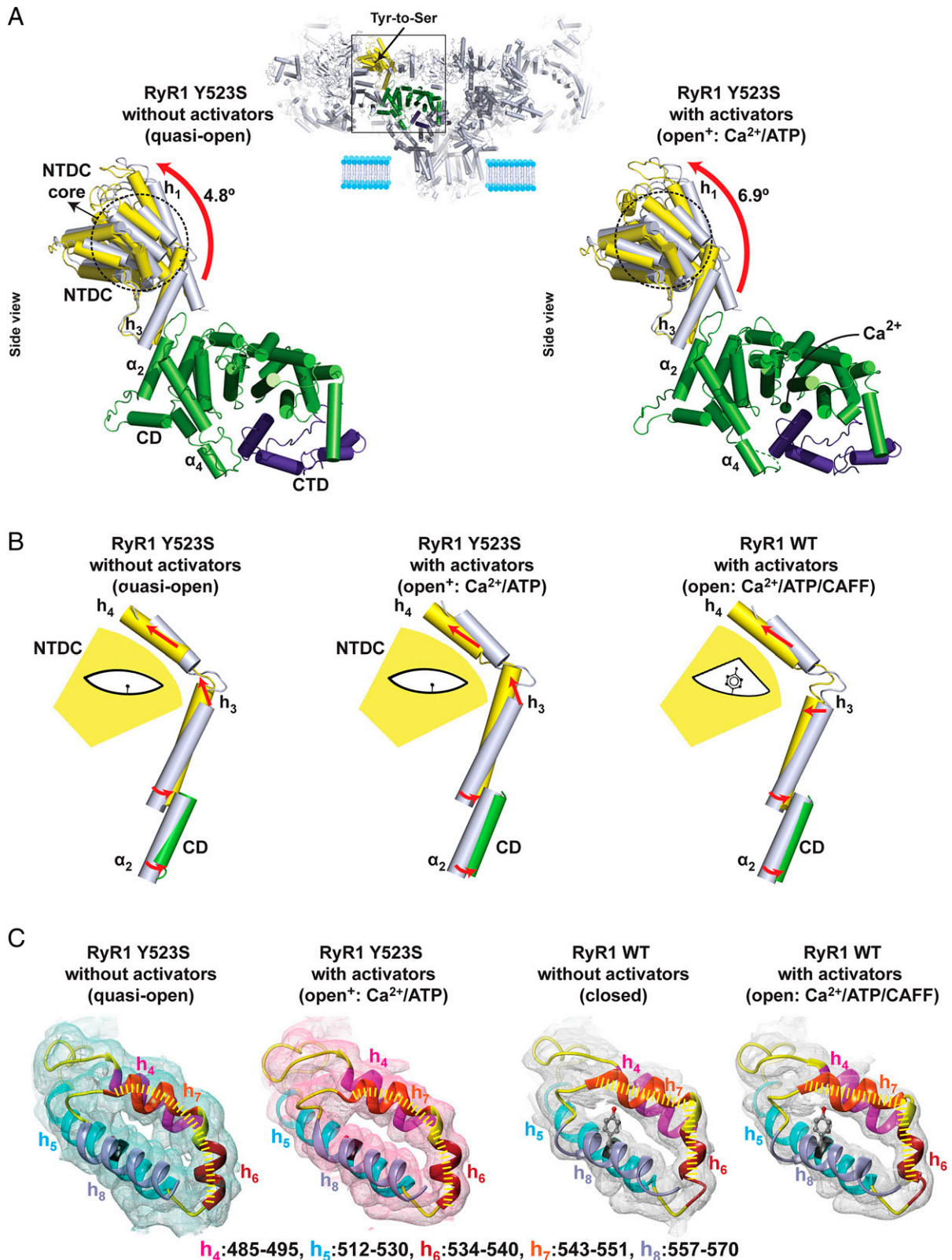
Fig. 3. The Y523S mutation causes the NTDC core to collapse in mutant RyR1. (*A*) The NTDC rocking by 4.8° and 6.9° in RyR1 Y523S quasi-open and open[+], respectively, caused by rearrangement of helices in the NTDC core (encircled with dashed black lines), caused partial closure of the Ca^{2+} binding site. Structure of RyR1 WT closed (PDB: 5TB0) is shown in gray cylinders. Helices h_1, h_3 of the NTDC and α_2, α_4 of the CD function as a ~100 Å lever. (*B*) Collapse of the NTDC core pulls h_4 and connected h_3 of the NTDC in RyR1 Y523S quasi-open and open[+]. The helix h_3 nudges α_2 of the CD, mimicking movement upon RyR1 WT channel opening. (*C*) Lack of the "spacer" Tyr523 residue leads to a change in angle between helices h_6 and h_7 in the NTDC of RyR1 Y523S quasi-open and open[+] as compared to RyR1 WT (dashed yellow lines) and compression of the interhelical space.

helix h_6 and h_7, giving rise to a continuous, bent helix h_6–h_7 in the RyR1 Y523S quasi-open structure (Fig. 3*C* and *SI Appendix,* Fig. S7*A*). The resolved kink involves an ~1.6 Å inward

movement of helix h_6–h_7 toward helix h_5 (*SI Appendix,* Fig. S7*A* and Movies S1 and S2). Essentially, the replacement of Tyr523, which acts as a spacer, to Ser523 results in forward displacement

of h_4 and collapse of the helices h_6 and h_7 toward the central space, thereby altering the original arrangement of helices $h_{3–8}$ (Fig. 3 and *SI Appendix*, Fig. S7).

The Mutation Alters the Tilt of a Newly Identified Lever Spanning from the RyR1 Surface to the Ca^{2+} Binding Site. The rearrangement of the NTDC core also has consequences on the rest of the channel, as helix h_3 of the NTDC has multiple interactions with helix α_2 of the CD. This interface is dominated by polar amino acid residues on both sides and the interactions between them are preserved despite gating, or despite the mutation (see circular *Insets* in *SI Appendix*, Fig. S8). The two helices are almost parallel, forming an angle that remains practically constant among closed WT, open WT (e.g., negligible relative rotation of ~1° compared with the 7° tilt of h_3), and quasi-open mutant RyR1 in WT (see rectangular *Insets* in *SI Appendix*, Fig. S8).

The role of the CD in channel opening is well established (25). Upon binding of Ca^{2+}, this domain, composed of 18 helices forming a helical repeat (Fig. 3*A*), undergoes squeezing and tilting, which induces relocation of multiple surrounding domains and results in channel opening. As described previously, the rearrangement of helices in the NTDC core caused by the mutation transmits from helix h_3 of NTDC to helix α_2 of the CD of the same subunit, and from there the conformational change is further transmitted to CD-α_4 (through CD-α_3; see red arrows in *SI Appendix*, Fig. S8 and Movie S3). As a result, the "push" by NTDC-h_3 sensed through CD-α_2 alters the conformation of the entire CD in a way that is similar to the one caused by Ca^{2+} binding, as described in greater detail in the next section.

Based on the fact that in WT the angle between CD-α_2 and NTDC-h_3 is preserved within 1° through the gating conformational change, we suggest that multiple connected α-helices (i.e., NTDC-h_4, NTDC-h_3, CD-α_2, and CD-α_4) function as a 100 Å-long lever that spans from the NTDC "antennae" to the distal side of the CD (*SI Appendix*, Fig. S8 and Movie S3) next to the Ca^{2+} binding site, which constitutes a pivotal point in RyR1. The aberrant tilting of this central lever within the CytA as a result of the mutation emerges as a main culprit of the altered communication between RyR1 and DHPR, and also appears to explain RyR1's increased sensitivity to Ca^{2+}.

The RyR1 Y523S Ca^{2+} Binding Site Gets Partially Activated in the Absence of Ca^{2+} and ATP. The combination of Ca^{2+} coordination and ATP binding induces RyR1 channel opening. The Ca^{2+} binding site of RyR1 lies at the interface of CD and CTD with negatively charged and polar residues from both domains (i.e., Glu3893, Glu3967 from CD and Thr5001, His5002 from CTD). Coordination of Ca^{2+} closes the cavity around the cation and triggers opening (21, 26). Upon Ca^{2+} binding, the carbonyls of E3967 and Thr5001 approach from 10.1 Å to 8.1 Å. In the RyR1 Y523S open$^+$ structure (obtained in the presence of Ca^{2+}), we see unambiguous density for a Ca^{2+} ion coordinated with Glu3893, Glu3967, and Thr5001 (Fig. 4*A* and *SI Appendix*, Fig. S9*A*). The distances between the backbone carbonyl of Thr5001 and the Cα atom of E3967 are 10.1 Å in WT closed, 8.1 Å in WT open, and 8.2 Å in mutant open (*SI Appendix*, Fig. S9*A*). Its CTD lifted by ~2.2 Å, also comparable to the 2.5 Å for RyR1 WT under open-state conditions (Fig. 4*A* and *SI Appendix*, Fig. S9*A*).

When compared with RyR1 under closed-state conditions, the Ca^{2+} binding site of RyR1 Y523S undergoes subtle partial closure, which brings the backbone O-atom of Thr5001 25%

closer to the negatively charged carbonyl O-atoms of Glu3967 (*SI Appendix*, Fig. S9*A*). In addition, the CTD of RyR1 Y523S lifts up by ~1.0 Å, which is almost halfway toward the 2.5 Å usually seen in WT channel opening (Fig. 4*A* and *SI Appendix*, Fig. S9*A*). It is worth emphasizing that compression of the Ca^{2+} binding site occurs in the absence of Ca^{2+} ions, and that this phenomenon is similar to the effect reported for the MH/CCD RyR1 R164C mutation (17).

The ATP binding site is located in a nook created by the U-motif, CTD, and the S6 helix (21, 26). The ATP binding site in the RyR1 Y523S quasi-open map (obtained in the absence of ATP) was empty, whereas the RyR1 Y523S open$^+$ map clearly displays the density corresponding to the added ATP (Fig. 4*B* and *SI Appendix*, Fig. S9*B*). In the RyR1 Y523S open$^+$ structure, negatively charged phosphate groups of ATP interact with positively charged Lys4214, Lys4211, and Arg4215 of the U-motif, while the hydrophobic adenosine moiety interacts with Phe4959, Ile4960, and Phe4975 of the CTD (*SI Appendix*, Fig. S9*B*), in a similar configuration to RyR1 WT open. Thus, the interaction of ATP with RyR1 was unaltered by the mutation. Of note, the mutation-induced preactivation of RyR1 takes place in the absence of both Ca^{2+} and ATP.

The Pore Is Marginally Affected by the Mutation. The channel of RyR1 Y523S under closed-state conditions remained closed, with a radius of 1.0 Å at the gating residue Ile4937 (Fig. 4*D* and *E* and *SI Appendix*, Table S2). This finding indicates that the channel remains nonconducting in the absence of Ca^{2+}, which agrees with the normal control of skeletal muscle movement in individuals with the mutation (12); even when considering heterozygosity, a small fraction of RyR1s would have four mutant subunits.

Under open-state conditions, the conduction pathway of RyR1 Y523S open$^+$ had a similar profile to that of RyR1 WT except for a dilation to 5.4 Å at the gating residue compared with 4.4 Å in RyR1 WT under open-state conditions (Fig. 4 and *SI Appendix, Table S2*). The open state was achieved in the presence of only endogenous activators (Ca^{2+} and ATP), unlike the reference RyR1 WT that required the addition of an exogenous activator, caffeine (5 mM) (21). Notably, a fully open state was attained at just ~1.5 μM free Ca^{2+}, which is in agreement with the more than 10-fold enhanced Ca^{2+} sensitivity of RyR1 Y523S (14). It is also noteworthy that gating occurs under such a narrow range of Ca^{2+} concentrations.

Spherical densities were present in the pore of the RyR1 Y523S open$^+$ structure close to Asp4945, Gln4933, and in the selectivity filter area (*SI Appendix*, Fig. S9*C*). Although these densities were not visible beyond 4σ and hence are most likely to be water molecules, the periodicity of their appearance is striking and corresponds to densities that we observed in other RyR1 WT reconstructions (26) as well as in other ion channels (27).

Interestingly, we identified distinct tubular densities in the RyR1 Y523S quasi-open structure, nestled between the S6 and S5 helices of one subunit and S4 of the adjacent subunit (Fig. 4*C*). Although the densities were not strong enough to be modeled, they appear to correspond to long alkyl chains of a lipid molecule, which was likely 1-palmitoyl-2-oleoyl-glycero-3-phosphocholine (POPC) that was used in the reconstitution in nanodiscs. We previously modeled phosphatidyl choline in the same crevice for RyR1 WT under inactivated conditions (26). Of note, this density is not visible in the RyR1 Y523S open$^+$ structure with the crevice appearing empty, which is also in agreement with our previous data indicating absence of lipids in open RyR1 (26).
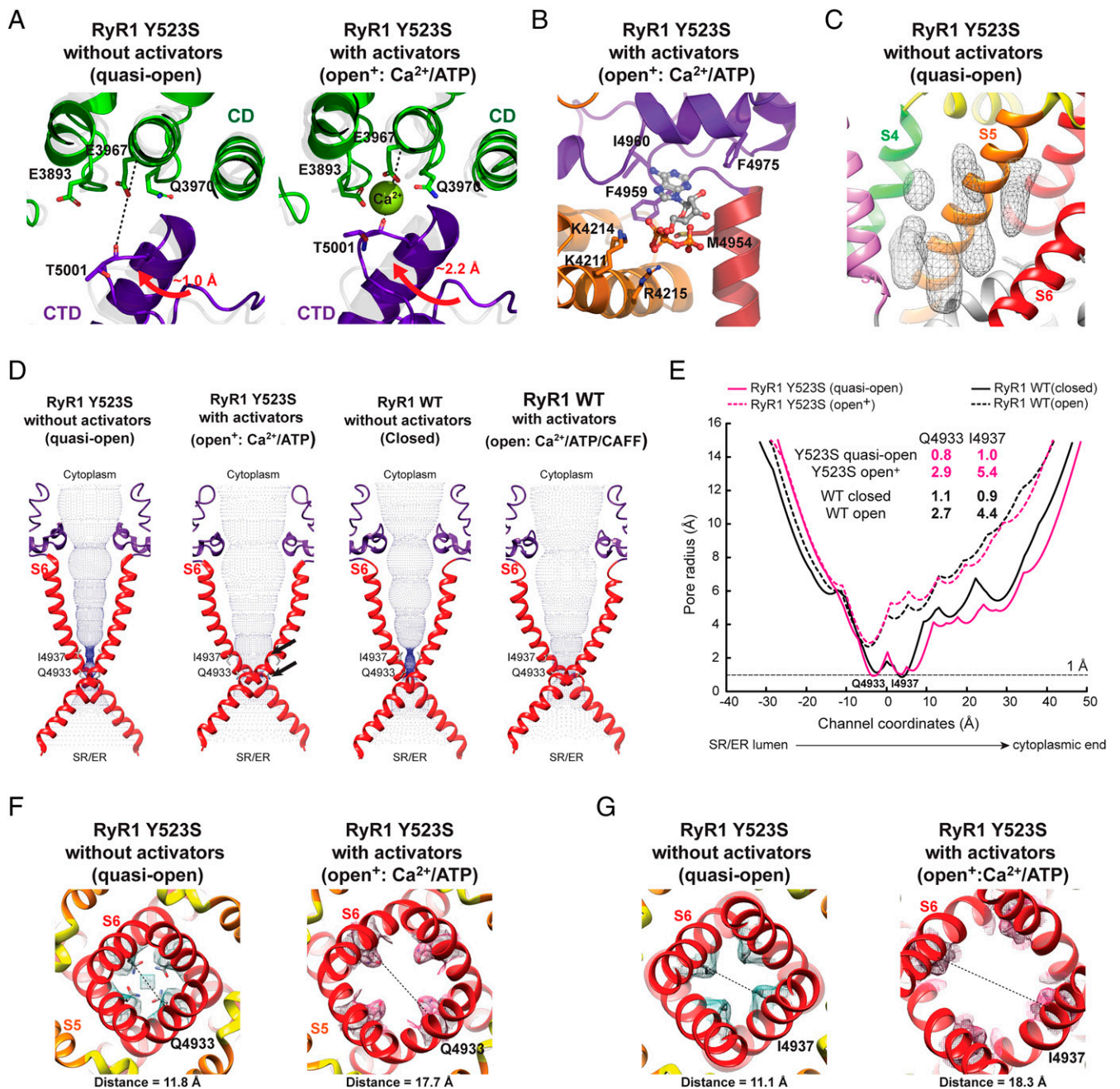
Fig. 4. Ca^{2+} and ATP binding sites and TmD of RyR1 Y523S quasi-open and open+ structures. (*A*) Under closed-state, Ca^{2+} free conditions, the Ca^{2+} binding site undergoes partial closure in RyR1 Y523S, as substantiated by the ~1.2 Å lift (red arrow) of the CTD (indigo ribbons) toward CD (green ribbons) of the same subunit. In the presence of Ca^{2+}, RyR1 Y523S open+ showed density corresponding to Ca^{2+} coordinated to Glu3893, Glu3967, and Gln3970 of CD (green ribbons) and with the backbone O atom of Thr5001 in the CTD (indigo ribbons) at the Ca^{2+} binding site. RyR1 WT closed is shown in transparent gray ribbons. (*B*) ATP bound to the RyR1 Y523S open+ structure at the interface between the U-motif domain, CTD, and S6 helix of the same subunit. (*C*) Tubular densities suggestive of lipids in a crevice between S6, S5, and S4 helices of an adjacent subunit in the TmD of RyR1 Y523S quasi-open. (*D*) Under closed-state conditions, the channel pore lined with S6 helices of the four subunits remains closed (RyR1 Y523S quasi-open). Under open-state conditions, the pore is fully open in RyR1 Y523S open+ and shows greater dilation at Ile4937 and Gln4933 (indicated by black arrows). (*E*) Pore radius along the z axis measured from the luminal side. Pore radii at the hydrophobic gate (Ile4937) and at the secondary constriction site (Gln4933) for the different reconstructions are indicated at the *Top* of the graph in angstroms. (*F* and *G*) Distances between Cα atoms of diagonally opposite residues at the two sites of constriction (distances and residues indicated in the figure) of RyR1 Y523S quasi-open.

Discussion

In this study, we solved the structure of an MH- and CCD-causing Y522S (rabbit Y523S) RyR1 mutant in both the open (1.5 μM free Ca^{2+}, 5 mM ATP) and closed (2 mM EGTA) states at ~4.0 Å resolution. The Y522S mutation in RyR1 is one of the most studied among the more than 200 RyR1 mutations identified thus far (28). We have shown that in the absence of activators, the Y523S mutation in the NTDC of

RyR1 resulted in changes that were transmitted throughout the CytA to varying extents (Figs. 1 and 2). In RyR1 WT, through multiple hydrophobic interactions, Tyr523 acts as a spacer residue and maintains the optimum orientation of α-helices in the NTDC core (Fig. 3 and *SI Appendix,* Fig. S7). These interactions were absent in mutant RyR1, wherein the large aromatic phenol ring of Tyr was replaced by a smaller hydroxymethyl sidechain of Ser (Fig. 3 and *SI Appendix,* Fig. S7). This alteration collapsed the NTDC core and precipitated spontaneous

rocking of the entire NTDC (Figs. 1–3). This had a profound effect on several domains of the CytA (Figs. 1, 2, and 5), resulting in the quasi-open structure of RyR1 Y523S with a conformation halfway to the open state in the absence of activators.

Our findings suggest that the Y523S mutation affects mainly the closed state of the mutant channels, while the mutant channels under open-state conditions deviate less from the WT open conformation. The domains at the periphery of RyR1 undergo greater relocation in RyR1 Y523S open$^+$ as compared to RyR1 WT during channel opening (Figs. 1 and 2), which combined with the subtle pore dilation in RyR1 Y523S open$^+$ (Fig. 4), likely underlies the changes observed in channel gating and kinetics. Additionally, the homogeneous population of channels in the open conformation under the mild activation conditions of ~1.5 μM Ca^{2+} is in agreement with the larger open probabilities (P$_o$) (29) and increased Ca^{2+} sensitivity (14); this finding further demonstrates the effect of the Y523S mutation on the energy landscape of the channel. Besides increased sensitivity to Ca^{2+} activation, previous reports indicate that the Tyr-to-Ser mutation induces decreased Ca^{2+}-dependent inactivation (30), altogether resulting in higher cytosolic Ca^{2+} concentration and lower Ca^{2+} stored in the SR at rest; these effects account for the histological anomalies and muscle weakness that characterize CCD (12). Although the pore of RyR1 still can close in the Y523S mutant, its pathological significance relies on the decreased energy required to open the channel and its susceptibility to activation when volatile anesthetics such as halothane are administered (7).

Our previous structural determination of RyR1 with the MH/CCD R163C mutation (rabbit R164C) revealed an anomalous closed-state conformation of the CytA that was initiated by rocking of the NTDA domain containing the mutation, with a closed (albeit dilated) pore that agrees with functional studies (14, 17). The structure of another MH/CCD NTDC mutant (porcine RyR1 R615C) has been determined (31). Surprisingly, the pore of the RyR1 R615C mutant channel was open under closed-state conditions (5 mM EGTA). This structural finding contradicts functional results by the authors of that study and others (14) where RyR1 R615C is closed under these conditions, and the fact that the homozygous pig used for protein purification was viable. When the two mutations are compared side by side, RyR1 Y522S is significantly more severe than R615C as measured by several metrics as demonstrated in functional studies by multiple groups (14, 15, 32, 33); yet we demonstrate that RyR1 Y523S responds to closed-state conditions (2 mM EGTA). Thus, the suggestion that the pore of RyR1 R615C is open under closed-state conditions should be taken with caution, as it is possible that other factors unrelated to the mutation could have affected the structure of the channel.

The large and complex RyR1 channel is regulated by a wide variety of partners (proteins, ions, small molecules) as well as posttranslational modifications such as phosphorylation and oxidation. Among the various protein-binding partners, bidirectional coupling of RyR1 with DHPR is well characterized. EC coupling involves orthograde signaling from the DHPR to the RyR1 (34), with the α1 II-III loop of DHPR as the main proposed candidate (35), and its β-subunit and other protein partners as additional candidates (36–38) that physically couple with RyR1 and trigger its opening. While the regions of RyR1 that interact with DHPR remain elusive, several domains have been suggested, including residues 1,635 to 2,636 (within the handle domain) (39) as well as residues 2,659 to 3,720 (located in P2 and HD2) (36, 39, 40). A defining hallmark of the Y522S mutation is its increased sensitivity to DHPR activation

(via orthograde signaling) by shifting voltage-dependent Ca^{2+} release from the SR/ER to more hyperpolarized potentials, by ~40 mV (15, 16, 33). Additionally, the Y522S mutation has been reported to have an influence on retrograde signaling, the mechanism by which RyR1 controls activity of DHPR's electrophysiological properties in myotubes (41, 42) and in knockin mice (43). As revealed in our 3D structures, all of the putative DHPR-binding domains undergo large conformational changes in RyR1 Y523S quasi-open (i.e., obtained under closed-state conditions). Of special note is the core of the NTDC itself, which is rigid and protrudes toward the DHPR, forming four short antennae (one per subunit). The NTDC is connected rigidly through a set of α-helices that protrude in the opposite direction toward the transmembrane domain. These interconnected helices form four long levers (one per subunit) that reach 100 Å into the center of the RyR1, in close proximity to the Ca^{2+} binding site (Fig. 5 and *SI Appendix,* Fig. S8). In the mutant channel under closed-state conditions, the tilt of each of the four levers resembles that of WT RyR1 open (Fig. 5 and *SI Appendix,* Fig. S8 and Movie S3). The altered conformation of this long lever along with conformational changes in other DHPR-facing domains of RyR1 suggest that the levers might constitute a long-range conformational pathway of the DHPR–RyR1 protein complex.

Our growing work on structural effects of single-point mutations in RyRs, which includes the reported structure of mutant mammalian RyR1 and RyR2 (17), shows that while the end result of RyR1 disease mutations in different domains (previously determined NTDA and currently determined NTDC mutants) have a common denominator—large conformational changes mostly confined to the CytA—the means by which this is achieved at a molecular level is distinct. This difference underscores the continued importance of studying RyR single-point disease mutations structurally, aided by improvements in cryo-EM technology, and highlights the need for targeted therapy to correct these molecular anomalies.

Materials and Methods

Reagents. All reagents were purchased from Thermo Fisher Scientific or Sigma-Aldrich except for membrane scaffold protein 1E3D1 (MSP1E3D1) and POPC, which were purchased from Addgene and Avanti Polar Lipids, respectively.

Expression and Purification of RyR1 Y523S from HEK293 Cells. Purification of recombinant RyR1 Y523S from HEK293 cells was performed in accordance with previously published protocol (17, 20).
Cell culture and expression. Briefly, HEK293 cells expressing rabbit RyR1 Y523S were cultured on 150 mm dishes/plates using Dulbecco's modified Eagle medium (high glucose, glutamine, and no sodium pyruvate) supplemented with fetal bovine serum and bovine growth serum (Gibco, Thermo Fisher Scientific) and penicillin/streptomycin. Expression of RyR1 Y523S was induced using doxycycline (~1–2 μg/mL) 48 to 72 h before harvesting the cells for vesicle purification.
Vesicle purification. Harvested cells were pelleted by centrifugation (573 × *g*, 10 min) and ruptured by sonication. Subsequently, the vesicle fraction of the lysed cells was separated from the nuclei fraction and other debris by centrifugation (4,400 × *g*, 10 min), and the supernatant was subjected to ultracentrifugation (100,000 × *g*, 1 h) to pull down vesicles. The vesicle pellet was resuspended in 5 mM imidazole pH 7.4, 10% (wt/vol) sucrose, and protease inhibitor mixture (aprotinin [5 μg/mL], leupeptin [5 μg/mL], and pefabloc [2.5 μg/mL]) (protease inhibitor; PI) using a Dounce homogenizer. Vesicles were flash frozen using liquid N$_2$ and stored at −80 °C for subsequent protein purification.
Protein purification. Purified vesicles (freshly purified or thawed) were solubilized for 25 min at 4 °C with mild agitation in solubilization buffer (5% wt/vol 3-[(3-cholamidopropyl)dimethyl-ammonio]-1-propane sulfonate (CHAPS) and 1.25% wt/vol phosphatidylcholine (PC), 1 M NaCl, 20 mM Na-Mops pH 7.4, 2 mM dithiothreitol (DTT), and PI). Solubilized vesicles were subjected to
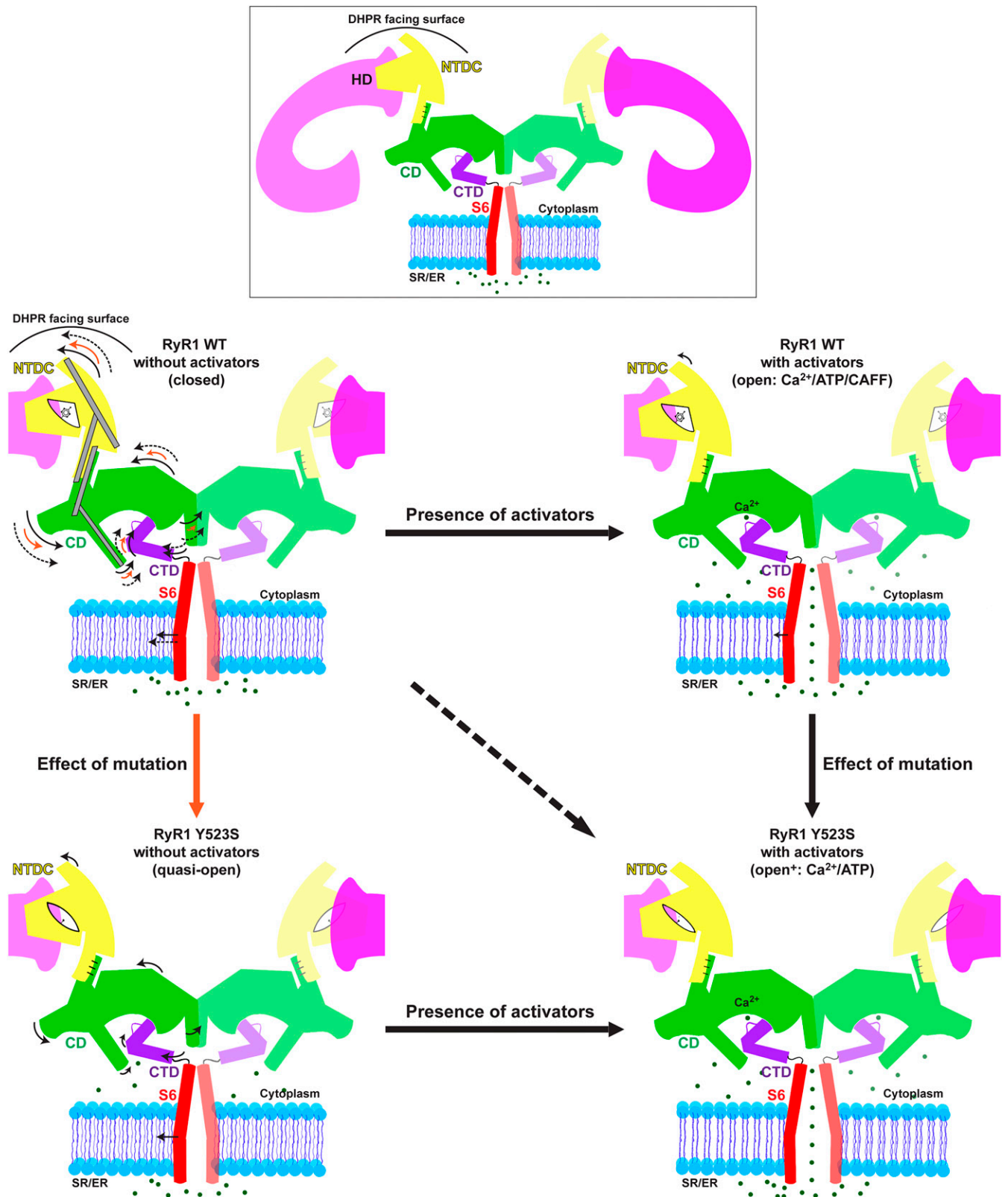
Fig. 5. Schematic representation of conformational changes in mutant RyR1 Y523S. The rearrangement of the NTDC core due to loss of a spacer residue, Tyr, causes spontaneous rocking of NTDC resulting in large-scale conformational changes in the CytA while the pore of the channel remains closed. The arrows within the *Top Left* indicate change of conformation during WT channel opening (solid black) and the effect of the mutation under closed-state conditions (orange). For comparison, the dashed black arrows illustrate the final altered open$^+$ conformation of Y523S. All movements are with respect to WT closed. Black arrows within the *Bottom Left* indicate change of conformation of Y523S during opening. Black arrows within the *Top Right* indicate extra movement that RyR1 Y523S open$^+$ (shown below) undergoes with respect to RyR1 WT open. Four rigid levers (one within each monomer, shown as gray cylinders in the *Top Left*) composed of connected α-helices (stabilized by interactions between NTDC-h$_3$ and CD-α$_2$) span a distance of 100 Å. These connect the DHPR-facing surface of the protein and the CD, modulating channel gating. For the sake of clarity only NTDC, CD, CTD, and S6 helices of RyR1 from two monomers in diagonal are shown.

ultracentrifugation (100,000 × *g* for 1 h) to separate insolubilized protein. The supernatant was layered onto the 10% sucrose layer of a discontinuous sucrose gradient (10%, 12%, 14%, 16%, 18%, and 20% [wt/vol]) and ultracentrifuged (120,000 × *g*, 23 h) using a swing bucket rotor. The layers were unmounted and subject to sodium dodecyl sulfate-polyacrylamide gel electrophoresis (SDS-PAGE) and stained with Coomassie Brilliant Blue to confirm the presence of RyRs. The pooled RyR-containing fractions were diluted fivefold using dilution buffer (20 mM Na-Mops pH 7.4, 0.5% wt/vol CHAPS, 0.125% wt/vol PC, 2 mM DTT, and PI) and concentrated using a HiTrap Heparin HP column (1 mL; Amersham Biosciences). RyRs bound to the column were first washed with wash buffer 1 (20 mM Na-Mops pH 7.4, 0.2 M NaCl, 0.5% wt/vol CHAPS, 0.125% wt/vol PC, 2 mM DTT, and PI), followed by wash buffer 2 (20 mM Na-Mops pH 7.4, 0.2 M NaCl, 0.015% wt/vol Tween-20, 2 mM DTT, and PI) and eluted in ~100 μL aliquots using elution buffer (20 mM Na Mops pH 7.4, 0.9 M NaCl, 0.015% wt/vol Tween-20, 2 mM DTT). Purity and quality of purified RyR1 Y523S were determined using SDS-PAGE and negative staining with 0.75% wt/vol uranyl formate. Aliquots of purified RyR1 Y523S were flash frozen using liquid N_2 and stored at −80 °C for subsequent cryo-EM grid preparation.

Reconstitution in Nanodiscs. RyR1 Y523S was reconstituted in nanodiscs prior to cryo-EM grid preparation as previously described (17). Purified rabbit RyR1 Y523S was incubated with MSP1E3D1 and POPC (1:2:50 RyR:MSP:POPC molar ratio) at 4 °C for 3 h. For the closed-state condition, detergent (Tween-20) was removed by dialysis in buffer containing 20 mM Na-Mops pH 7.4, 600 mM KCl, 2 mM DTT, and 2 mM EGTA at 4 °C. For the open-state condition, detergent was removed by dialysis in buffer containing 20 mM Na-Mops pH 7.4, 600 mM KCl, 2 mM DTT, and 50 μM CaCl$_2$. For both the closed- and open-state datasets, FKBP12.6 (10:1 FKBP:RyR molar ratio) was added to purified RyR1 Y523S. Additionally, for the open-state dataset, the channel was incubated with 5 mM ATP pH 7.4 for 2 h at 4 °C. Presence of ATP resulted in a free Ca^{2+} concentration of 1.5 μM as estimated with Maxchelator (https://somapp.ucdmc.ucdavis.edu/pharmacology/bers/maxchelator). The quality of RyR1 Y523S incorporated into lipid nanodiscs was assessed by negative staining with 0.75% wt/vol uranyl formate prior to cryo-EM grid preparation.

Cryo-EM Grid Preparation. Grid preparation was carried out as described previously (17) using an FEI Vitrobot Mark IV plunger. Quantifoil Au grids (1.2/1.3; 300 mesh; Quantifoil) were used without glow discharge. For both datasets, 2.0 μL of RyR1 Y523S-FKBP12.6 complex (~4.5 mg/mL) was adsorbed onto a Quantifoil Au grid followed by blotting (blot force 2 and blot time 1 to 1.5 s) using Whatman 540 filter paper and plunged into liquid ethane cooled by liquid N_2. Cryo-EM grids were screened on an in-house Tecnai F20 electron microscope and grids with optimal ice thickness, particle concentration, orientations, and distribution were used for data collection.

Data Collection. For the RyR1 Y523S closed- and open-state datasets, we collected 13,171 and 11,018 movies, respectively, on a Titan Krios at an accelerating voltage of 300 kV equipped with a post-Gatan Imaging filter (post-GIF) K3 direct electron detector. Data were collected at 81,000× magnification and 0.54 Å per pixel for both datasets using Leginon (44). The slit width for GIF was 20 eV. Exposure time was 3.12 s with an electron dose of 53 e$^-$/Å^2 spread over 40 frames and a defocus range of −0.7 to −2.5 μm for both datasets.

Image Processing. Around ~41% and ~22% of the RyR1 Y523S quasi-open and open$^+$ movies were purged due to a combination of various factors including issues in data collection such as mistargeting of the gold grid as well as misalignment of the energy filter slit resulting in 7,768 and 8,648 movies used for image processing and 3D reconstruction using cryoSPARC (45). Patch motion correction was followed by contrast transfer function (CTF) estimation. Around ~1,000 manually picked particles for each dataset were subjected to two-dimensional (2D) classification to generate reference classes. Template-based automated picking with three reference classes and further purging to remove false picks resulted in ~1.2 million picks for both datasets. These particles were subjected to four successive rounds of 2D classification to further remove false picks and junk particles, resulting in 154,814 and 197,530 particles for the quasi-open and open$^+$ datasets, respectively. Subsequent ab initio reconstruction into four classes for the RyR1 Y523S quasi-open and open$^+$ datasets gave two and one good classes, respectively. For the quasi-open dataset, particles

from the two good classes (141,098) were combined and subjected to 3D reconstruction using the nonuniform refinement functionality (46) with per-particle defocus refinement as well as global CTF refinement, resulting in a map with a resolution of 4.0 Å. Map quality was boosted by performing local refinement using a single monomer mask in cryoSPARC. Additionally, particle subtraction was performed to retain signal only from the NTD (A, B, and C) and SPRY (1 to 3) domains of a single subunit followed by local refinement in cryoSPARC to yield a map with better details. For the open$^+$ dataset, one good class of 84,954 particles was subjected to 3D reconstruction using the homogenous refinement function (45) with per-particle defocus refinement as well as global CTF refinement resulting in a map with a resolution of 4.05 Å. In this case, no further improvements were observed either with nonuniform refinement or with local refinement.

Model Building. A single subunit of rabbit RyR1 R164C (PDB: 6WOT) (17) with the Cys164 mutated back to Arg was used as an initial model for real space refinement in Phenix (47). The single subunit was aligned to the maps of RyR1 Y523S closed and open datasets in Chimera (48). After initial rounds of real-space refinement with Ramachandran and secondary structure restraints applied (47), the refined model of the single subunit was fitted manually using Coot (49) to each of the maps (closed- and open-state datasets) using the real space refine tool with Ramachandran restraints applied. Iterative rounds of refinement and manual fitting were performed till optimum model quality was achieved. Validation was performed as part of phenix.real_space_refine (47), and quality of models was assessed using MolProbity scores (50) (*SI Appendix*, Table S1). Since no density corresponding to the P2 domain was visible, the crystal structure of the domain (PDB: 3RQR) (51) was placed atop HD1 and no refinement or manual fitting was performed. The structure of the HD2 was updated based on reference structure (PDB: 7M6A) (52). For the quasi-open structure, the model was fitted either to the consensus map (4.0 Å resolution), to the single monomer, or to the NTD-SPRY map, using the best-quality electron density map for any given area.

Analysis of Structures. Measurements for individual domain movement (both translation and rotation) were performed using the angle_between_domains script in PyMOL (The PyMOL Molecular Graphics System, version 2.5.2 Schrödinger, LLC) for the domains of the cytoplasmic assembly. For the initial analysis, the entire TmD (residues 4,540 to 4,956) of a single monomer was considered as a single entity. For the individual helices in the TmD, movement (both translation and rotation) was measured in Chimera (48) using the axes/planes/centroids functionality after defining each axis. All resulting values for rotation (°) and translation (Å) were plotted in GraphPad Prism 9 (GraphPad Software) to generate the heat maps. Angle measurements (between NTDC-h$_3$ and CD-α$_2$, between NTDC-h$_3$ of mutant structures and RyR1 WT closed, and between CD-α$_2$ of mutant structures and RyR1 WT closed) were also performed in Chimera (48). All measurements were performed using Cα atoms only. Vector maps were generated using the modevectors.py script in PyMOL (The PyMOL Molecular Graphics System, version 2.0.0 Schrödinger, LLC). Interaction energies were calculated using the Amino Acid Interaction web server (53). Channel pore radius was calculated using HOLE2.11 (54); only the pore-lining S6 helices (residues 4,908 to 4,956) and CTD (residues 4,957 to 5,037) of all four subunits were retained. Fourier shell correlation and pore analysis plots were generated using gnuplot. Local resolution maps were generated using ResMap (55).

High-resolution images for figures were obtained using either PyMOL, Chimera (48), or ChimeraX (56).

Author affiliations: [a]Department of Physiology and Biophysics, School of Medicine, Virginia Commonwealth University, Richmond, VA 23298; [b]Purdue Cryo-EM Facility, College of Science, Purdue University, West Lafayette, IN 47907; and [c]Department of Cellular and Molecular Pharmacology, Juntendo University Graduate School of Medicine, Tokyo 113-8421, Japan

1. M. Samsó, A guide to the 3D structure of the ryanodine receptor type 1 by cryoEM. *Protein Sci.* **26**, 52–68 (2017).
2. G. Meissner, The structural basis of ryanodine receptor ion channel function. *J. Gen. Physiol.* **149**, 1065–1089 (2017).
3. J. T. Lanner, Ryanodine receptor physiology and its role in disease. *Adv. Exp. Med. Biol.* **740**, 217–234 (2012).
4. R. T. Dirksen, G. Avila, Distinct effects on Ca^{2+} handling caused by malignant hyperthermia and central core disease mutations in RyR1. *Biophys. J.* **87**, 3193–3204 (2004).
5. K. A. Quane et al., Mutations in the ryanodine receptor gene in central core disease and malignant hyperthermia. *Nat. Genet.* **5**, 51–55 (1993).
6. R. Robinson, D. Carpenter, M. A. Shaw, J. Halsall, P. Hopkins, Mutations in RYR1 in malignant hyperthermia and central core disease. *Hum. Mutat.* **27**, 977–989 (2006).
7. H. Rosenberg, N. Pollock, A. Schiemann, T. Bulger, K. Stowell, Malignant hyperthermia: A review. *Orphanet J. Rare Dis.* **10**, 93 (2015).
8. M. E. Kolb, M. L. Horne, R. Martz, Dantrolene in human malignant hyperthermia. *Anesthesiology* **56**, 254–262 (1982).
9. A. Ward, M. O. Chaffman, E. M. Sorkin, Dantrolene. A review of its pharmacodynamic and pharmacokinetic properties and therapeutic use in malignant hyperthermia, the neuroleptic malignant syndrome and an update of its use in muscle spasticity. *Drugs* **32**, 130–168 (1986).
10. H. Jungbluth, Central core disease. *Orphanet J. Rare Dis.* **2**, 25 (2007).
11. S. Treves, H. Jungbluth, F. Muntoni, F. Zorzato, Congenital muscle disorders with cores: The ryanodine receptor calcium channel paradigm. *Curr. Opin. Pharmacol.* **8**, 319–326 (2008).
12. K. A. Quane et al., Mutation screening of the RYR1 gene in malignant hyperthermia: Detection of a novel Tyr to Ser mutation in a pedigree with associated central cores. *Genomics* **23**, 236–239 (1994).
13. W. J. Durham et al., RyR1 S-nitrosylation underlies environmental heat stroke and sudden death in Y522S RyR1 knockin mice. *Cell* **133**, 53–65 (2008).
14. T. Murayama et al., Divergent activity profiles of type 1 ryanodine receptor channels carrying malignant hyperthermia and central core disease mutations in the amino-terminal region. *PLoS One* **10**, e0130606 (2015).
15. G. Avila, R. T. Dirksen, Functional effects of central core disease mutations in the cytoplasmic region of the skeletal muscle ryanodine receptor. *J. Gen. Physiol.* **118**, 277–290 (2001).
16. M. G. Chelu et al., Heat- and anesthesia-induced malignant hyperthermia in an RyR1 knock-in mouse. *FASEB J.* **20**, 329–330 (2006).
17. K. A. Iyer et al., Structural mechanism of two gain-of-function cardiac and skeletal RyR mutations at an equivalent site by cryo-EM. *Sci. Adv.* **6**, eabb2964 (2020).
18. T. Murayama et al., Genotype-phenotype correlations of malignant hyperthermia and central core disease mutations in the central region of the RYR1 channel. *Hum. Mutat.* **37**, 1231–1241 (2016).
19. A. Uehara et al., Extensive Ca2+ leak through K4750Q cardiac ryanodine receptors caused by cytosolic and luminal Ca2+ hypersensitivity. *J. Gen. Physiol.* **149**, 199–218 (2017).
20. Y. Hu et al., Purification of recombinant wild type and mutant ryanodine receptors expressed in HEK293 cells. *Bio Protoc.* **11**, e4112 (2021).
21. A. des Georges et al., Structural basis for gating and activation of RyR1. *Cell* **167**, 145–157.e17 (2016).
22. M. Samsó, W. Feng, I. N. Pessah, P. D. Allen, Coordinated movement of cytoplasmic and transmembrane domains of RyR1 upon gating. *PLoS Biol.* **7**, e85 (2009).
23. W. Peng et al., Structural basis for the gating mechanism of the type 2 ryanodine receptor RyR2. *Science* **354**, aah5324 (2016).
24. T. W. E. Steele, M. Samsó, The FKBP12 subunit modifies the long-range allosterism of the ryanodine receptor. *J. Struct. Biol.* **205**, 180–188 (2019).
25. X. C. Bai, Z. Yan, J. Wu, Z. Li, N. Yan, The Central domain of RyR1 is the transducer for long-range allosteric gating of channel opening. *Cell Res.* **26**, 995–1006 (2016).
26. A. R. Nayak, M. Samsó, Ca^{2+} inactivation of the mammalian ryanodine receptor type 1 in a lipidic environment revealed by cryo-EM. *eLife* **11**, e75568 (2022).
27. S. Oh, N. Paknejad, R. K. Hite, Gating and selectivity mechanisms for the lysosomal K^+ channel TMEM175. *eLife* **9**, e53430 (2020).
28. T. A. Lawal, E. S. Wires, N. L. Terry, J. J. Dowling, J. J. Todd, Preclinical model systems of ryanodine receptor 1-related myopathies and malignant hyperthermia: A comprehensive scoping review of works published 1990–2019. *Orphanet J. Rare Dis.* **15**, 113 (2020).
29. J. T. Lanner et al., AICAR prevents heat-induced sudden death in RyR1 mutant mice independent of AMPK activation. *Nat. Med.* **18**, 244–251 (2012).
30. C. Manno et al., Altered Ca^{2+} concentration, permeability and buffering in the myofibre Ca^{2+} store of a mouse model of malignant hyperthermia. *J. Physiol.* **591**, 4439–4457 (2013).
31. K. A. Woll, O. Haji-Ghassemi, F. Van Petegem, Pathological conformations of disease mutant ryanodine receptors revealed by cryo-EM. *Nat. Commun.* **12**, 807 (2021).
32. M. Brini et al., Ca^{2+} signaling in HEK-293 and skeletal muscle cells expressing recombinant ryanodine receptors harboring malignant hyperthermia and central core disease mutations. *J. Biol. Chem.* **280**, 15380–15389 (2005).
33. R. Lefebvre et al., Defects in Ca^{2+} release associated with local expression of pathological ryanodine receptors in mouse muscle fibres. *J. Physiol.* **589**, 5361–5382 (2011).
34. E. Rios, G. Brum, Involvement of dihydropyridine receptors in excitation-contraction coupling in skeletal muscle. *Nature* **325**, 717–720 (1987).
35. A. F. Dulhunty et al., Activation and inhibition of skeletal RyR channels by a part of the skeletal DHPR II-III loop: Effects of DHPR Ser687 and FKBP12. *Biophys. J.* **77**, 189–203 (1999).
36. W. Cheng, X. Altafaj, M. Ronjat, R. Coronado, Interaction between the dihydropyridine receptor Ca^{2+} channel beta-subunit and ryanodine receptor type 1 strengthens excitation-contraction coupling. *Proc. Natl. Acad. Sci. U.S.A.* **102**, 19225–19230 (2005).
37. R. T. Rebbeck et al., The β(1a) subunit of the skeletal DHPR binds to skeletal RyR1 and activates the channel via its 35-residue C-terminal tail. *Biophys. J.* **100**, 922–930 (2011).
38. J. M. Eltit, C. Franzini-Armstrong, C. F. Perez, Amino acid residues 489–503 of dihydropyridine receptor (DHPR) β1a subunit are critical for structural communication between the skeletal muscle DHPR complex and type 1 ryanodine receptor. *J. Biol. Chem.* **289**, 36116–36124 (2014).
39. J. Nakai, N. Sekiguchi, T. A. Rando, P. D. Allen, K. G. Beam, Two regions of the ryanodine receptor involved in coupling with L-type Ca^{2+} channels. *J. Biol. Chem.* **273**, 13403–13406 (1998).
40. S. Sencer et al., Coupling of RYR1 and L-type calcium channels via calmodulin binding domains. *J. Biol. Chem.* **276**, 38237–38241 (2001).
41. J. Nakai et al., Enhanced dihydropyridine receptor channel activity in the presence of ryanodine receptor. *Nature* **380**, 72–75 (1996).
42. R. A. Bannister, K. G. Beam, Ryanodine modification of RyR1 retrogradely affects L-type Ca^{2+} channel gating in skeletal muscle. *J. Muscle Res. Cell Motil.* **30**, 217–223 (2009).
43. Z. Andronache, S. L. Hamilton, R. T. Dirksen, W. Melzer, A retrograde signal from RyR1 alters DHP receptor inactivation and limits window Ca^{2+} release in muscle fibers of Y522S RyR1 knock-in mice. *Proc. Natl. Acad. Sci. U.S.A.* **106**, 4531–4536 (2009).
44. C. Suloway et al., Automated molecular microscopy: The new Leginon system. *J. Struct. Biol.* **151**, 41–60 (2005).
45. A. Punjani, J. L. Rubinstein, D. J. Fleet, M. A. Brubaker, cryoSPARC: Algorithms for rapid unsupervised cryo-EM structure determination. *Nat. Methods* **14**, 290–296 (2017).
46. A. Punjani, H. Zhang, D. J. Fleet, Non-uniform refinement: Adaptive regularization improves single-particle cryo-EM reconstruction. *Nat. Methods* **17**, 1214–1221 (2020).
47. D. Liebschner et al., Macromolecular structure determination using X-rays, neutrons and electrons: Recent developments in Phenix. *Acta Crystallogr. D Struct. Biol.* **75**, 861–877 (2019).
48. E. F. Pettersen et al., UCSF Chimera–A visualization system for exploratory research and analysis. *J. Comput. Chem.* **25**, 1605–1612 (2004).
49. P. Emsley, B. Lohkamp, W. G. Scott, K. Cowtan, Features and development of Coot. *Acta Crystallogr. D Biol. Crystallogr.* **66**, 486–501 (2010).
50. C. J. Williams et al., MolProbity: More and better reference data for improved all-atom structure validation. *Protein Sci.* **27**, 293–315 (2018).
51. P. Sharma et al., Structural determination of the phosphorylation domain of the ryanodine receptor. *FEBS J.* **279**, 3952–3964 (2012).
52. Z. Melville, K. Kim, O. B. Clarke, A. R. Marks, High-resolution structure of the membrane-embedded skeletal muscle ryanodine receptor. *Structure* **30**, 172–180.e3 (2022).
53. J. Galgonek, J. Vymetal, D. Jakubec, J. Vondrášek, Amino Acid Interaction (INTAA) web server. *Nucleic Acids Res.* **45**, W388–W392 (2017).
54. O. S. Smart, J. G. Neduvelil, X. Wang, B. A. Wallace, M. S. Sansom, HOLE: A program for the analysis of the pore dimensions of ion channel structural models. *J. Mol. Graph.* **14**, 354–360, 376 (1996).
55. A. Kucukelbir, F. J. Sigworth, H. D. Tagare, Quantifying the local resolution of cryo-EM density maps. *Nat. Methods* **11**, 63–65 (2014).
56. E. F. Pettersen et al., UCSF ChimeraX: Structure visualization for researchers, educators, and developers. *Protein Sci.* **30**, 70–82 (2021).
57. K. A. Iyer, Y. Hu, T. Murayama, M. Samso, Rabbit RyR1 disease mutant Y523S in complex with FKBP12.6 embedded in lipidic nanodisc in the closed state. Protein Data Bank. https://www.rcsb.org/structure/7T64. Deposited 13 December 2021.
58. K. A. Iyer, Y. Hu, T. Murayama, M. Samso, Rabbit RyR1 disease mutant Y523S in complex with FKBP12.6 embedded in lipidic nanodisc in the open state. Protein Data Bank. https://www.rcsb.org/structure/7T65. Deposited 13 December 2021.
59. K. A. Iyer, Y. Hu, T. Murayama, M. Samso, Rabbit RyR1 disease mutant Y523S in complex with FKBP12.6 embedded in lipidic nanodisc in the closed state. EMDB. https://www.ebi.ac.uk/emdb/EMD-25709. Deposited 13 December 2021.
60. K. A. Iyer, Y. Hu, T. Murayama, M. Samso, Rabbit RyR1 disease mutant Y523S in complex with FKBP12.6 embedded in lipidic nanodisc in the open state. EMDB. https://www.ebi.ac.uk/emdb/EMD-25710. Deposited 13 December 2021.